Sensors and Materials, Vol. 35, No. 12 (2023) 4177–4202
MYU Tokyo

S & M 3475

Highly Sensitive Amperometric Hydrazine Sensor Developed from Gold Nanoparticles Electrodeposited on Glassy Carbon Electrode Modified with Graphene Oxide and Poly(3,4-ethylenedioxythiophene): poly(styrenesulfonate) Composite

Hemas Arif Rahman,[1] Budi Riza Putra,[2] Mohamad Rafi,[1,3] Rudi Heryanto,[1,3] Chika Takai-Yamashita,[4,5] Yutaka Ohya,[4] and Wulan Tri Wahyuni[1,3*]

[1]Department of Chemistry, Faculty of Mathematics and Natural Sciences, IPB University, Bogor, West Java 16680, Indonesia
[2]Research Center for Metallurgy, National Research and Innovation Agency, South Tangerang 15315, Banten, Indonesia
[3]Tropical Biopharma Research Center, Institute of Research and Community Empowerment, IPB University, Indonesia
[4]Department of Chemistry and Biomolecular Science, Gifu University, 1-1 Yanagido, Gifu City 501-1193, Japan
[5]Institute of Multidisciplinary Research for Advanced Materials, Tohoku University, Katahira 2-1-1, Aoba-ku, Sendai 980-8577, Japan

(Received September 5, 2023; accepted November 8, 2023)

Keywords: gold nanoparticles, electrodeposition, hydrazine, sensor, voltammetry

Here, we demonstrate the development of a hydrazine sensor using gold nanoparticles (AuNPs) electrodeposited on the surface of a glassy carbon electrode (GCE) modified with the material composite of graphene oxide (GO) and poly(3,4-ethylenedioxythiophene):poly(styrenes ulfonate) (PEDOT:PSS). The morphological, electrochemical, and structural properties of this developed hydrazine sensor were characterized by Raman spectroscopy, Fourier-transform infrared spectroscopy (FTIR), X-ray diffraction (XRD), electrochemical impedance spectroscopy (EIS), scanning electron microscopy (SEM), and atomic force microscopy (AFM). Cyclic voltammetry and amperometry techniques have been used to investigate the electrochemical behavior and electroanalytical performance of this proposed sensor, and obtained an excellent result in terms of its analytical parameters. A linear range of 0.2−100 μM was obtained from the amperometric detection of hydrazine using this developed sensor. The detection and quantitation limits of this proposed hydrazine sensor were calculated as 0.005 and 0.08 μM, respectively. Furthermore, this proposed sensor for hydrazine detection exhibited good reproducibility and stability with a relative standard deviation (%RSD) of less than 5%. In addition, this developed sensor for hydrazine detection also exhibited good selectivity in the presence of several interferences, including $NaNO_2$, $FeSO_4$, $Zn(CH_3CO_2)_2$, NH_4NO_3, chlorophenol, triclosan, and ascorbic acid, as well as it depicted %recovery values of 93–104%.

*Corresponding author: e-mail: wulantriws@apps.ipb.ac.id
https://doi.org/10.18494/SAM4640

ISSN 0914-4935

In conclusion, this platform sensing based on a AuNPs/GO/PEDOT:PSS-modified GCE for hydrazine detection shows excellent electroanalytical performance and could potentially be employed for real applications.

1. Introduction

In recent years, the approach of metal electrodeposition on the electrode surface to fabricate a highly sensitive electrochemical sensor has been extensively investigated with the purpose of detecting electroactive molecules or species.[1–4] To develop highly sensitive electrochemical sensors, gold nanoparticles (AuNPs) are one of the widely used electrode modifiers owing to their attractive characteristics such as good biocompatibility, increased electrocatalytic activity, and chemical stability, as well as they provide an enhanced specific surface area.[5–7] In addition, AuNPs can be readily functionalized with various nanomaterials to be developed as gold-based nanocomposites for electrochemical sensors such as AuNPs–carbon nanomaterials,[8] AuNPs–metal oxide,[9] AuNPs–metal dichalcogenide,[10] AuNPs–metal organic framework,[11] AuNPs–imprinted polymer,[12,13] and AuNPs–polymer-metal oxide.[14,15] As a result, researchers were able to make research progress with an innovative approach for the detection of electroactive species by employing these nanocomposites as sensor materials with improved sensitivity, selectivity, and stability.

Among several techniques to modify the electrode surface, electrodeposition is a fast and efficient process to synthesize AuNPs to improve their specific properties such as electrical conductivity,[16] electrocatalytic activity,[17] and chemical and mechanical stabilities.[18] The amount and size of metal nanoparticles deposited on the electrode surface can be easily controlled by changing the number of cycles during electrodeposition. Another important benefit of utilizing this process is that homogeneity can be significantly improved by the specific potential electrodeposition of metal nanoparticles to avoid the presence of impurities on the electrode surface.[19] Controlling the electrodeposition parameters such as the number of cycles, working voltage, and deposition time could also produce various types of metal nanoparticle with different morphologies or structures.[20]

Previously, we reported on the synergy between composite materials consisting of reduced graphene oxide with poly(3,4-ethylenedioxythiophene):poly(styrenesulfonate) (PEDOT:PSS) as electrode modifiers to enhance the sensitivity of the modified electrodes.[21] A combination between graphene oxide and conductive polymer may be utilized as an electrode modifier that exhibits improved electrocatalytic activity and conductivity to be employed as an electrochemical sensor.[22–25] In addition, hydrazine has attracted increasing attention for the development of an electrochemical sensor based on the modified electrodes owing to its properties as one of the electroactive substances.[26,27] Hydrazine is an important precursor that has been frequently utilized in pharmaceutical intermediates, agriculture, food storage, and fuel cells.[28] However, the excessive usage of hydrazine in the environment may pollute water sources owing to its toxicity and carcinogenic effect to human health.[29] In addition, our previously proposed hydrazine sensor has shown several good analytical performance characteristics, including sensitivity, stability, and selectivity for potential interferences, with its results compared with

those of the standard spectrophotometric technique.[30] Nevertheless, it is still important to develop a more sensitive electrochemical sensor for hydrazine detection by electrodepositing gold nanoparticles (AuNPs) on the surface of the graphene oxide and PEDOT:PSS composite. The presence of gold nanoparticles on the surface of a modified electrode can enhance the sensitivity towards hydrazine detection.[31] To the best of our knowledge, the electrodeposition of gold on the surface of a glassy carbon electrode (GCE) modified with the graphene oxide (GO) and PEDOT:PSS composite for hydrazine detection has not been reported.

2. Experimental Methods

2.1 Reagents and apparatus

Poly(3,4-dioxythiophene)-poly(styrene-4-sulphonate) (PEDOT:PSS) (CAS: 155090-83-8), graphite (CAS: 155090-83-8), H_2SO_4, $KMnO_4$, H_2O_2 30%, Na_2HPO_4, NaH_2PO_4, KCl, hydrazine dihydrochloride (CAS: 5341-61-7), $NaNO_2$, $FeSO_4$, $Zn(CH_3CO_2)_2$, NH_4NO_3, chlorophenol, triclosan, and ascorbic acid were purchased from Sigma-Aldrich Ltd. and used without further purification.

Electrochemical experiments were conducted using PalmSens Emstat 3 (ES316U669) equipped with PSTrace 5.9 for cyclic voltammetry and differential pulse voltammetry investigations. Electrochemical impedance spectroscopy (EIS) analysis was performed using a PalmSens 4.0 Potensiostat (PalmSens, Houten, The Netherlands). The Raman spectra of graphite and graphene oxide materials were obtained from a Horiba LabRAM HR Evolution Micro Confocal Hyperspectral 3D Imaging Raman Spectrometer. The infrared spectra of graphene oxide and conductive polymer were obtained from an FT/IR-4600 JASCO spectrometer. X-ray diffraction (XRD) characterizations of graphene oxide and conductive polymer were performed using a Rigaku Ultima IV X-ray diffractometer (monochromatic CuKα irradiation, λ = 1.54 Å) with the voltage and current kept at −40 kV and 30 mA, respectively. SEM–energy-dispersive X-ray spectroscopy (SEM-EDS) images were taken using an FEI Quanta 650 FEG SEM system. In this work, all electrochemical experiments were performed in a three-electrode system consisting of a 3-mm-diameter glassy carbon electrode (GCE) (IJ Cambria Scientific) as the working electrode, silver/silver chloride (3 M) as the reference electrode, and a platinum wire as the auxiliary electrode. The voltammetric data obtained from electrochemical experiments were processed and displayed using Origin Pro 7.0 (OriginLab, Northampton, USA).

2.2 Modification of GCE with GO/PEDOT:PSS composite and gold (Au) electrodeposition

Graphene oxide (GO) was synthesized using the modified Hummer's method with some modifications to obtain the GO powder. The obtained GO powder was further characterized by Raman spectroscopy. Then, the GO powder was mixed with PEDOT:PSS (2 mg mL^{-1} in deionized water) at a weight ratio of 1:1. The GO/PEDOT:PSS composite solution was sonicated for 1 h and stirred for 1 h subsequently. Then, about 5 μL of this composite solution was drop-casted onto the surface of GCE (Fig. 1) and dried in an oven at 80 °C for 5 min. Next, gold

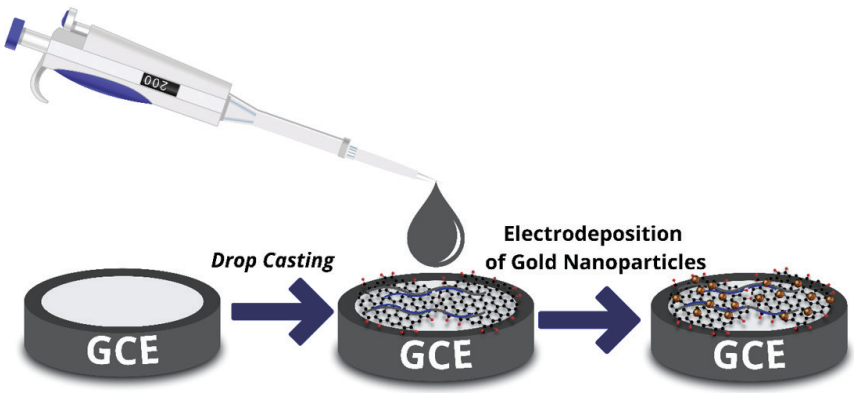

Fig. 1. (Color online) Schematic of the fabrication of gold nanoparticles (AuNPs) electrodeposited on GO/PEDOT:PSS-modified GCE.

nanoparticles (AuNPs) were electrodeposited on the GO/PEDOT:PSS composite by scanning 0.001 M $HAuCl_4 \cdot 3H_2O$ in 0.5 M H_2SO_4 in the potential range from 1.0 to −0.3 V (vs Ag/AgCl). Scanning was performed at a rate of 100 mV s^{-1} for 15 cycles to obtain electrodes (AuNPs/GO/PEDOT:PSS-modified GCE). The modified electrodes were then washed with deionized water and dried at room temperature (25 ± 2 °C). GO/PEDOT:PSS was characterized by FTIR and XRD, whereas AuNPs/GO/PEDOT:PSS was further characterized by SEM-EDS. Figure 1 shows a schematic of the preparation of AuNPs electrodeposited on the GO/PEDOT:PSS-modified GCE.

2.3 Evaluation of electrochemical behavior of AuNPs/GO/PEDOT:PSS/GCE

The electroanalytical performance of the modified electrode (AuNPs/GO/PEDOT:PSS-modified GCE) was evaluated by cyclic voltammetry (CV). The assessment of the electrochemical behavior of the modified electrode was performed using 1.0 mM $K_3[Fe(CN)_6]$ in 0.1 M phosphate buffer (pH 7) by CV. CV analysis was performed in the potential range from −0.4 to +0.9 V (vs Ag/AgCl) at a scan rate of 100 mV s^{-1} in triplicates. The GO/PEDOT:PSS-modified and AuNPs/GO/PEDOT:PSS-modified GCEs as the modified electrodes were compared with a bare GCE in terms of electrochemical performance. In addition, the conductivities of these three electrodes were compared by EIS to obtain the charge transfer resistance from each electrode. Next, these electrodes were employed for the measurement of 1.5 mM hydrazine hydrochloride in 0.1 M phosphate buffer (pH 7). The measurements were conducted by CV in the potential range from −0.30 to +0.85 V (vs Ag/AgCl) at a scan rate of 100 mV s^{-1} in triplicates.

2.4 Evaluation of electroanalytical performance of AuNPs/GO/PEDOT:PSS-modified GCE for hydrazine measurements

The modified electrode (AuNPs/GO/PEDOT:PSS-modified GCE) was evaluated by measuring the stock solution of hydrazine hydrochloride in the concentration range of 0.2–100 μM. The stock solution of hydrazine was prepared in 0.1 M phosphate buffer (pH 7) and measured by the chronoamperometric technique at a fixed potential of 0.12 V (vs Ag/AgCl) for 500 s in triplicates. Linearity was evaluated on the basis of the coefficient of determination (R^2) obtained from the regression linear equation. On the other hand, the limit of detection (LOD) and the limit of quantitation (LOQ) were determined using the signal-to-noise (S/N) ratio specifically for LOD ($S/N \approx 3$) and LOQ ($S/N \approx 10$). Sensitivity was determined from the slope of linear regression from the hydrazine measurements. Selectivity was determined from the recovery values of hydrazine current response before and after the addition of interference species. Interference species in the concentration ratio of 1:1, such as $NaNO_2$, $FeSO_4$, $Zn(CH_3CO_2)_2$, NH_4NO_3, chlorophenol, triclosan, and ascorbic acid, were added into 30 μM hydrazine hydrochloride in 0.1 M phosphate buffer (pH 7). Reproducibility was investigated by preparing six of the AuNPs/GO/PEDOT:PSS-modified GCEs and employed for the measurement of 30 μM hydrazine hydrochloride in 0.1 M phosphate buffer (pH 7). In addition, stability was examined by measuring the 30 μM hydrazine hydrochloride in 0.1 M phosphate buffer (pH 7) over six consecutive days using an amperometric technique.

2.5 Analysis of real samples

The hydrazine concentration in tap and drinking water was investigated using the standard addition technique. A standard calibration curve of hydrazine was prepared in the concentration range of 0.2–100 μM in 0.1 M phosphate buffer (pH 7). To determine the hydrazine concentration in real samples, samples of tap and drinking water were spiked with hydrazine and measured by the amperometric technique in triplicates. The hydrazine concentration obtained by the electrochemical technique was then compared with that obtained by the spectrophotometric technique according to the standard method.[30] In the spectrophotometric studies, a series of hydrazine concentrations from 0.2 to 3.81 μM with the addition of *para*-dimethylamino benzaldehyde and concentrated HCl were prepared. The absorbance of the solution was measured using a UV–Vis spectrophotometer at a maximum wavelength of 458 nm. The concentrations of hydrazine obtained by both electrochemical and spectrophotometric techniques were compared with its recovery values using Student's *t*-test at a significance level of 95%.

3. Results and Discussion

3.1 AuNPs/GO/PEDOT:PSS-modified GCE

One of the nondestructive methods to obtain a large amount of information about carbon-based materials is Raman spectroscopy. Figure 2(a) shows the Raman spectra of graphite and GO. There are several peaks in the Raman spectrum of graphite, i.e., D (1348 cm^{-1}), G (1576 cm^{-1}), and 2D (2688 cm^{-1}) bands. The D band in the Raman spectrum of carbon-based materials is typically associated with defects in graphite materials, which might be due to the existence of vacancies, dislocations, or fractures in the graphene layer.[32] Moreover, the G band originates from the in-plane vibration of sp^2-hybridized carbon atoms constituted in the graphene layers.[33] The last band (2D) is simply associated with the number of graphene layers. In addition, the successful conversion from graphite to GO can be confirmed by dividing the intensity ratios of the D band with the G band (I_D/I_G) and the 2D band with the G band (I_{2D}/I_G) from each material.[34] It can be seen that the I_D/I_G ratio increases from 0.24 (graphite) to 1.03 (GO), indicating the increasing number of defects present in the material, whereas the I_{2D}/I_G ratio decreases owing to the loss of graphene layers, which could be attributed to the conversion of graphite to GO. Therefore, it can be concluded that GO has been successfully obtained from graphite owing to

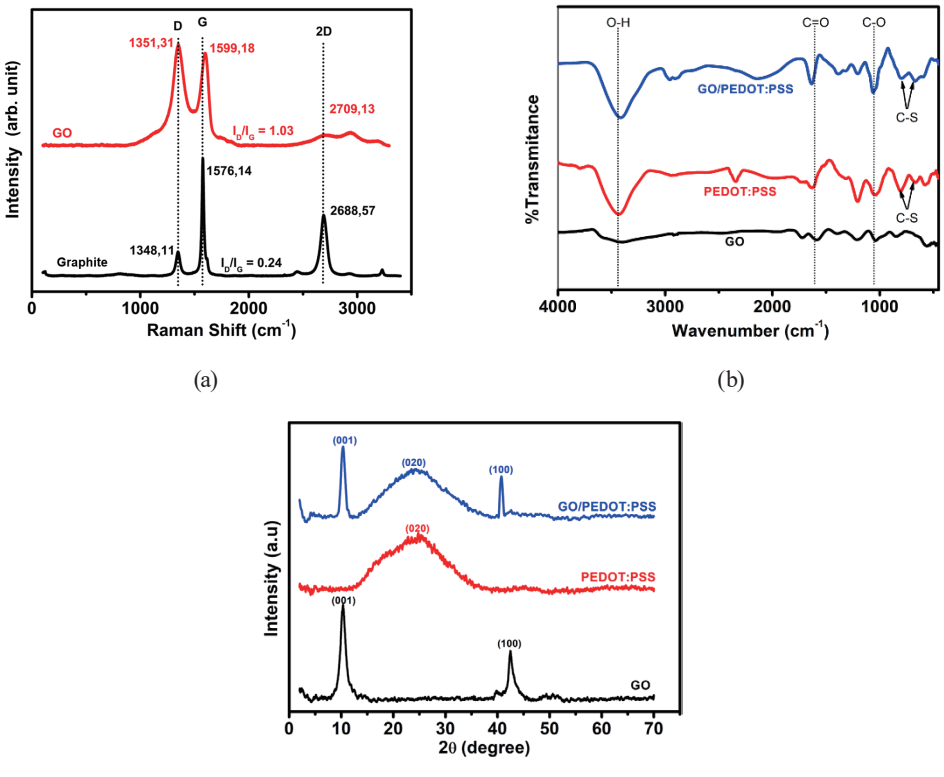

(a) (b)

(c)

Fig. 2. (Color online) (a) Raman spectra of graphite and GO, (b) FTIR spectra of GO, PEDOT:PSS, and the composite of GO/PEDOT:PSS, and (c) diffractograms of GO, PEDOT:PSS, and the composite of GO/PEDOT:PSS.

the exfoliation of graphene layers. GO could potentially be mixed with PEDOT:PSS as a conductive polymer to be employed as sensor materials.

FTIR spectroscopy was applied to identify the surface functional groups of GO and PEDOT:PSS as well as to confirm the chemical interactions in the composite of GO/PEDOT:PSS. Figure 2(b) shows the FTIR spectra obtained from GO, PEDOT:PSS, and the GO/PEDOT:PSS composite. The IR spectra for GO show vibration peaks at 3470 cm^{-1} (O–H stretching), 1714 cm^{-1} (C=O stretching), 1587 cm^{-1} (C=C stretching), and 1042 cm^{-1} (C–O stretching). Moreover, both FTIR spectra for PEDOT:PSS and its composite (GO/PEDOT:PSS) reveal vibration peaks at 1737 and 1627 cm^{-1} (C=C stretching in the thiophene backbone), 1198 and 1046 cm^{-1} (S–O stretching), and 810 and 659 cm^{-1} (C–S stretching).[35] It is clear that all the spectra obtained from IR analysis are similar, indicating the successful incorporation of PEDOT:PSS into the GO structure. In addition, it can be inferred from the IR spectra that GO is not functionalized during the composite preparation as no additional peak is observed.

X-ray diffraction (XRD) was carried out to investigate the interlayer space (*d*-spacing) of GO and the composite of GO/PEDOT:PSS. Figure 2(c) shows the diffractogram obtained from GO, PEDOT:PSS, and the composite of GO/PEDOT:PSS. From this figure, the XRD spectrum of GO shows two distinct peaks at $2\theta = 10.38$ and 42.28°. These two peaks are associated with the (001) and (100) diffractions of the GO sheet with their interlayer *d*-spacing values being calculated using Bragg's law [Eq. (1), where $n = 2$ and $\lambda = 1.54$ Å[36]] to be 8.52 and 2.12 Å, respectively. Moreover, PEDOT:PSS displays a characteristic peak at $2\theta = 24.33°$ related to the (020) diffraction plane, which can be attributed to the backbone of the PEDOT:PSS polymer.[37] However, since there is no visible sharp peak in its XRD spectrum and only a broad peak displayed at 25º, it can be associated with the amorphous structure of PSS and the interchain planar ring-stacking distance $d_{(010)}$ of PEDOT.[38] When GO was mixed with PEDOT:PSS, several characteristic peaks (2θ) appeared in its XRD spectrum at 10.27 and 42.96°, and thus their interlayer *d*-spacing can be calculated as 8.61 and 2.27 Å, respectively. The slight increase in interlayer *d*-spacing at $2\theta \approx 10.3$ and 42.3° in the GO/PEDOT:PSS composite can be associated with the good interaction between the GO layers and PEDOT:PSS owing to their π-π interactions.[39] Additionally, the inclusion of PEDOT:PSS in between GO layers can occur, which is expected to improve the conductivity of its composite.[40]

$$2d \sin\theta = n\lambda \tag{1}$$

It has been reported recently that hydrazine can be detected using a GCE modified with a composite of graphene oxide and PEDOT:PSS.[41] However, for future practical applications, its sensitivity for hydrazine detection still needs to be enhanced. One way to achieve this goal is by modifying metal nanoparticles, i.e., gold by electrodeposition on the surface of the modified GCE. Figure 3(a) shows the cyclic voltammogram of a 0.5 M H_2SO_4 solution containing 1 mM $HAuCl_4$ at a scan rate of 100 mV s^{-1} using the GO/PEDOT:PSS-modified GCE obtained in 15 cycles. This preliminary work was intended to obtain the optimum conditions for the electrodeposition of AuNPs on the surface of the GO/PEDOT:PSS-modified GCE. On the first cycle of the forward scan [Fig. 3(a)], a single reduction peak was observed at 0.48 V (vs Ag/

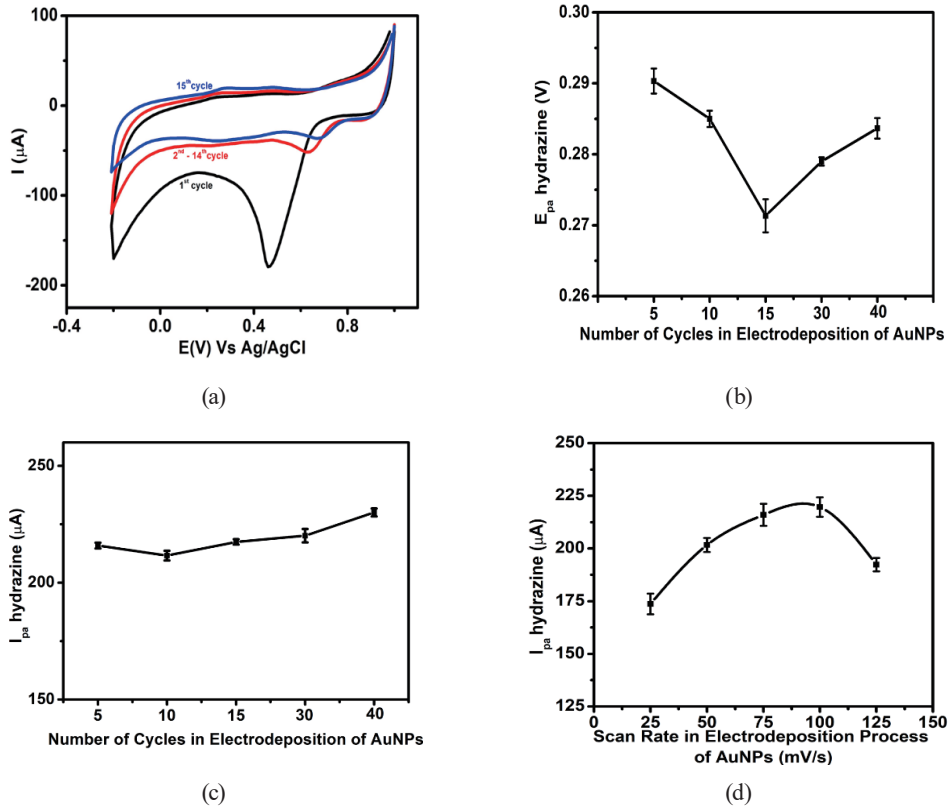

Fig. 3. (Color online) (a) Cyclic voltammogram of GO/PEDOT:PSS-modified GCE in the presence of 1 mM $HAuCl_4$ in 0.5 M H_2SO_4, (b) effect of number of cycles on the oxidation potential (E_{pa}) of 1.5 mM hydrazine in AuNPs/GO/PEDOT:PSS-modified GCE, (c) current response (I_{pa}) of 1.5 mM hydrazine at a scan rate of 100 mV s^{-1}, and (d) effects of different scan rates on the current response of 1.5 mM hydrazine in AuNPs/GO/PEDOT:PSS-modified GCE.

AgCl), and its intensity diminished until 15 cycles. This peak can be associated with the reduction of $AuCl_4^-$ involving three electrons into metallic gold on the surface of the modified electrode as outlined in Eqs. (2) and (3).

$$AuCl_4^- \rightarrow Au^{3+} + 4Cl^- \tag{2}$$

$$Au^{3+} + 3e^- \rightarrow Au \tag{3}$$

However, when the forward scan was continued from the 2nd cycle to the 15th cycle, it can be seen that this reduction peak shifted to a higher potential of approximately 160 mV. In addition, the intensity of the peak current for gold reduction after the 15th cycle did not significantly change even though the electrodeposition process continued until 40 cycles (figure not shown). This phenomenon is consistent with thermodynamics, which predicts that the growth of previously formed AuNPs occurs more easily than the nucleation of new nanoparticles on the surface of the modified electrode.[42] This is because the energy required for gold deposition is

relatively lower on previously formed AuNPs than on the new area on the surface of the modified electrode.[43] Thus, it can be deduced that the greater number of cycles during gold electrodeposition will result in the increase in the size of the gold nanoparticles as well.[44] Therefore, it is necessary to optimize the parameters during gold electrodeposition to still maintain the nanometer size of the nanoparticles. The optimized parameters will be employed for hydrazine detection using electrodeposited AuNPs on the composite of the GO/PEDOT:PSS-modified GCE.

The effects of the number of cycles and scan rate during AuNP electrodeposition on hydrazine oxidation were also investigated by CV using the GO/PEDOT:PSS-modified GCE. Figure 3(b) shows the effect of the number of cycles using the modified electrode (AuNPs/GO/PEDOT:PSS/GCE) on the peak of oxidation potential (E_{pa}) of 1.5 mM hydrazine in 0.1 M phosphate buffer (pH 7) at a scan rate of 100 mV s^{-1}. Each measurement of hydrazine oxidation using the modified electrode in different cycles of AuNP electrodeposition was performed in triplicates. As shown in this figure, the oxidation peak of hydrazine shifted negatively as the number of cycles increased from 5 to 15 with the lowest potential of hydrazine oxidation obtained at 15 cycles (E_{pa} = 0.27 V). After 15 cycles of AuNP electrodeposition, the potential peak of hydrazine shifted positively up to 40 cycles. On the basis of this result, it is preferable to choose the low potential peak for hydrazine (0.27 V) for practical applications owing to the lower risk of interference. In addition, according to Fig. 3(c), with the increasing number of cycles for AuNP electrodeposition, the current response of hydrazine oxidation slightly increased as well. However, since the current response of hydrazine oxidation, as well as time efficiency, did not significantly change after 15 cycles, we decided to choose 15 cycles as the optimum parameter of AuNP electrodeposition for further studies. In addition, as shown in Fig. 3(d), the highest peak current of hydrazine oxidation was obtained when the measurement was performed at a scan rate of 100 mV s^{-1} for AuNP electrodeposition in 15 cycles by CV. Therefore, the condition for AuNP electrodeposition on the GO/PEDOT:PSS-modified GCE in 15 cycles and at a scan rate of 100 mV s^{-1} was employed for subsequent experiments.

3.2 Characterization of surface of modified electrode using SEM-EDS and AFM techniques

The surface morphologies of the GO/PEDOT:PSS composite and AuNPs/GO/PEDOT:PSS were investigated by SEM with elemental mapping (EDX spectrum). Figure 4(a) reveals the surface morphology of the GO/PEDOT:PSS composite, which appears to be rough and flaky with a crumpled sheet-like structure. It is expected that this wrinkled surface of the GO/PEDOT:PSS composite would increase the surface area of the modified electrode as well as provide active sites for gold deposition. In addition, the EDX spectrum shown in the inset of Fig. 4(a) reveals that the GO/PEDOT:PSS composite contains 64.5% C, 31.5% O, and 3.9% S. Furthermore, from the elemental mapping of this composite shown in Fig. 4(c), it is clear that C, O, and S are uniformly distributed on the surface of the GO/PEDOT:PSS composite. When gold was electrodeposited on the surface of the GGO/PEDOT:PSS composite, the spherical AuNPs can be seen as small bright spots in Fig. 4(b) under 5000 times magnification.

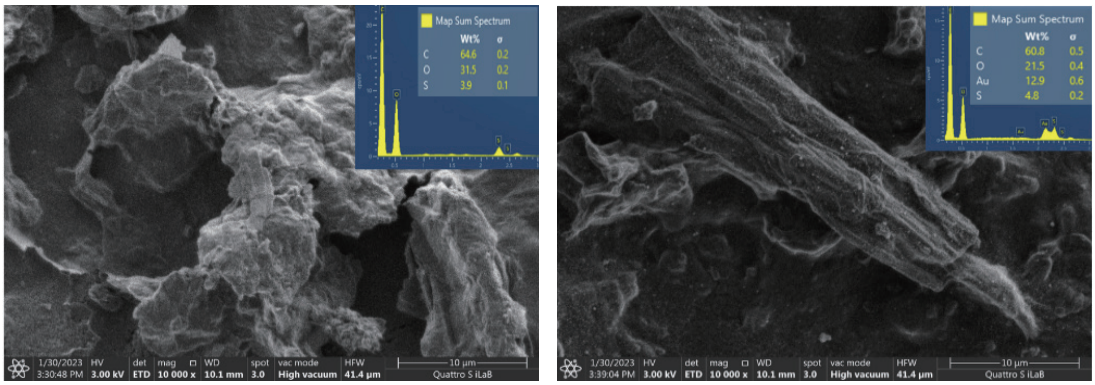

(a) (b)

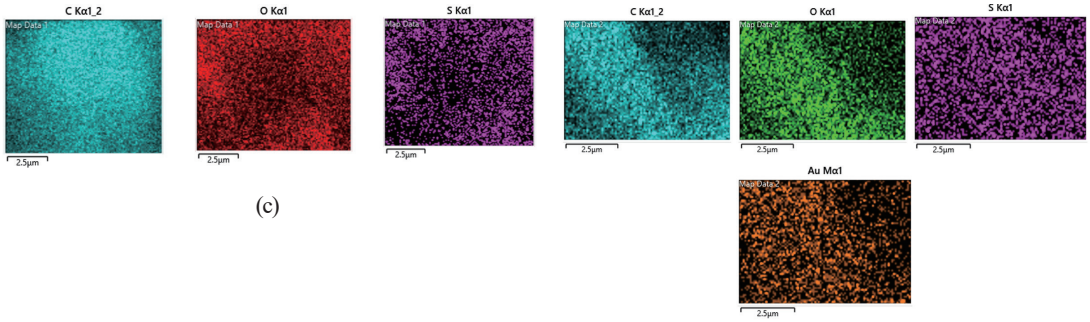

(c)

(d)

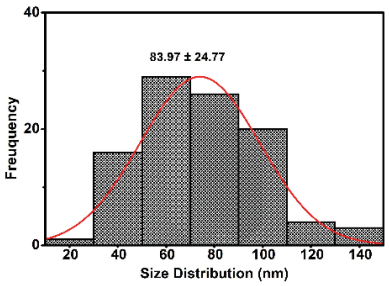

(e)

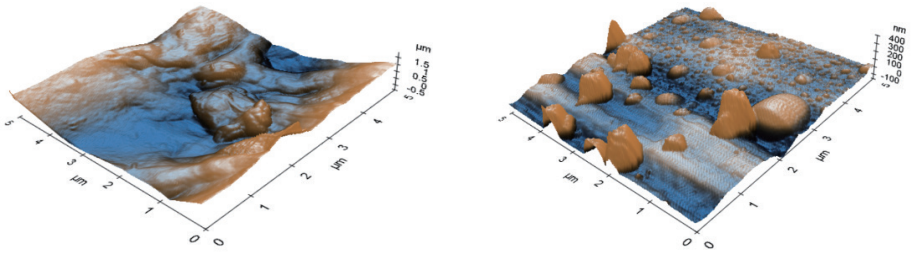

(f) (g)

Fig. 4. (Color online) (a) SEM image of GO/PEDOT:PSS composite, inset: distribution of elements (C, O, and S) in GO/PEDOT:PSS composite, (b) SEM image of AuNPs/GO/PEDOT:PSS, inset: distribution of elements (C, O, S, and Au) in AuNPs/GO/PEDOT:PSS, (c) elemental mapping of C, O, and S in GO/PEDOT:PSS composite, (d) elemental mapping of C, O, S, and Au in AuNPs/GO/PEDOT:PSS composite, (e) size distribution of gold electrodeposited on GO/PEDOT:PSS calculated using ImageJ software, and (f) AFM images of the composite of GO/PEDOT:PSS (left) and AuNPs/GO/PEDOT:PSS (right), which were obtained with a scan rate of 0.75 Hz.

As described in the previous reports[45], the mechanism of AuNP electrodeposition on the surfaces of graphene-based electrodes as determined by CV can be deduced in several steps. First, the reduction of Au^{3+} from the $AuCl_4^-$ precursor solution occurred at a potential near +0.4 V (vs Ag/AgCl), and Au^0 subsequently deposited on the graphene-based electrode surface rich in oxygen functional groups.[46] This process is initially generated by the formation of seeds of Au core, followed by the growth of AuNPs.[47] Furthermore, the EDX spectrum and elemental mapping of the surface of gold electrodeposited as shown in Figs. 4(b) and 4(d) on GO/PEDOT:PSS confirm the homogenous distribution of AuNPs with the elemental composition of C, O, S, and Au being 60.8, 21.8, 4.8, and 12.9 wt%, respectively. In addition, we also calculated the size distribution of gold electrodeposited on the surface of the GO/PEDOT:PSS composite in Fig. 4(e) using ImageJ software from 100 particles with the average size of AuNPs being 83.97 ± 24.77 nm. Nevertheless, to obtain clear and consistent evidence of the growth of AuNPs on the electrode surface, it is intriguing to further investigate the AuNPs/GOPEDOT:PSS surface using more advanced techniques such as AFM.

AFM was employed not only to characterize the surface morphologies but also to confirm the formation of AuNPs on the surface of the modified electrode. Figure 4(f) shows the surface morphologies obtained from GO/PEDOT and AuNPs/GO/PEDOT:PSS in a three-dimensional structure with a scan area of 5 × 5 μm^2. In Fig. 4(f) (left side), we can observe that the surface of GO/PEDOT:PSS is slightly rough and can be expressed in terms of the root-mean-square (RMS) roughness for this composite of 0.43 μm. However, when gold was electrodeposited (indicated by orange spheres) on the surface of the GO/PEDOT:PSS composite as shown in Fig. 4(f) (right side), a marked change in roughness was observed with its RMS of roughness increasing significantly to 60.44 μm. Additionally, we can easily observe in this figure that the size of the AuNP spheres in the initial seed stage is approximately less than 50 nm with some of the AuNP spheres having grown to more than 100 nm in size. These observations provide both qualitative and quantitative proofs of the formation of AuNPs on the surface of GO/PEDOT:PSS, either in the seed or growth stage. In addition, AuNPs behave as an electron transfer channel on the surface of the modified electrode, contributing to a large accessible surface area for the electrocatalytic reaction of analytes.[48,49] Furthermore, it is expected that the presence of AuNPs on the surface of the material composite will enhance the electrode conductivity for sensing applications.

3.3 Electrochemical behavior of AuNPs electrodeposited on GO/PEDOT:PSS-modified GCE for hydrazine detection

The electrochemical behaviors of electrodes (bare, GO/PEDOT:PSS-modified, and AuNPs/GO/PEDOT:PSS-modified GCEs) were evaluated for the measurement of 1.5 mM hydrazine in 0.1 M phosphate buffer (pH 7) in the potential range from 0 to 1.0 V. Figure 5(a) shows the corresponding voltammograms from the electrodes at a scan rate of 100 mV s^{-1} by CV with the oxidation potential of hydrazine observed at 0.44 V (vs Ag/AgCl) for the GO/PEDOT:PSS-modified GCE. However, when AuNPs were electrodeposited on the surface of the GO/PEDOT:PSS-modified GCE, the oxidation potential of hydrazine shifted to 0.27 V (vs Ag/AgCl).

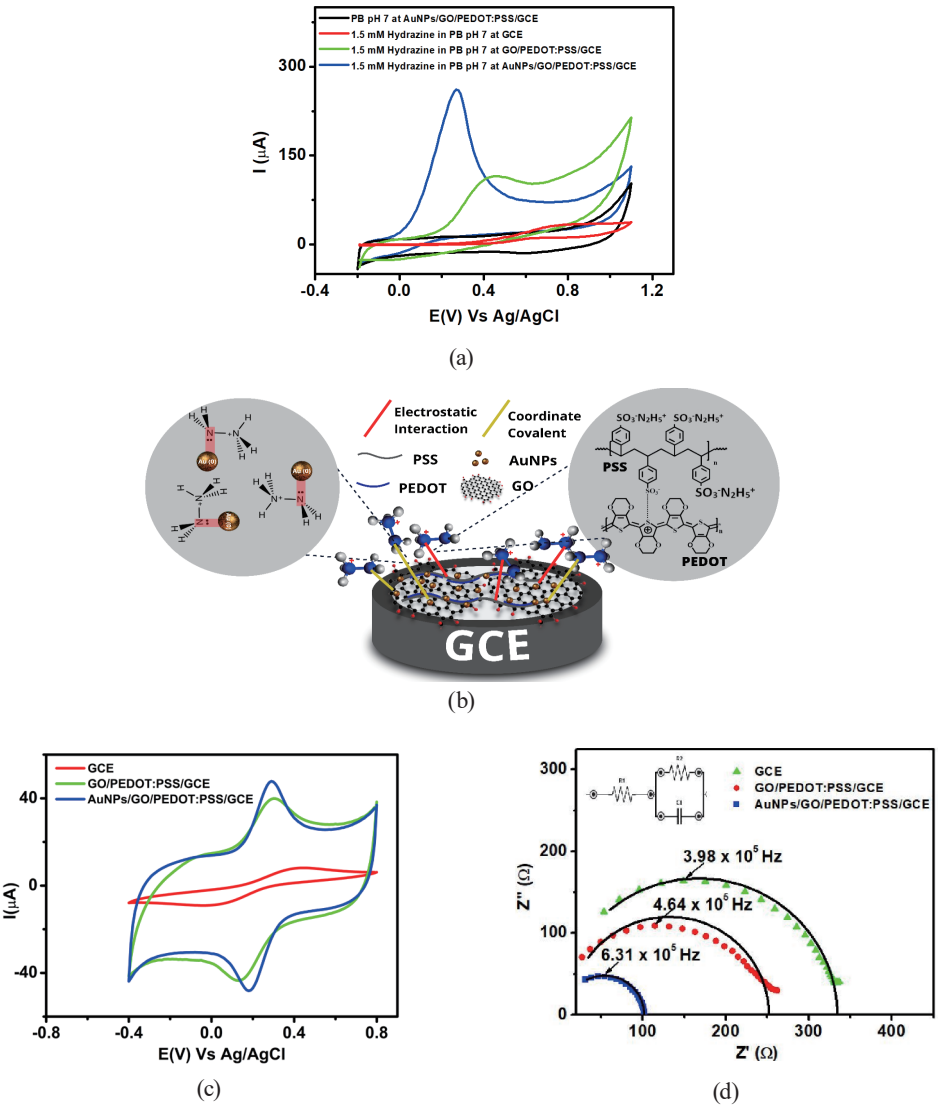

Fig. 5. (Color online) (a) Cyclic voltammogram obtained from the measurement in 0.1 M phosphate buffer (pH 7) containing 1.5 mM hydrazine at a scan rate of 50 mV s^{-1} using different modified electrodes, (b) interaction between the hydrazinium cation with AuNPs electrodeposited on the surface of GO/PEDOT:PSS-modified GCE, (c) cyclic voltammograms at 100 mV s^{-1}, and (d) Nyquist plot obtained from three different electrodes (bare, GO/PEDOT:PSS-modified, and AuNPs/GO/PEDOT:PSS-modified GCEs) for the measurement of 1 mM $K_3[Fe(CN)_6]$ in 0.1 M phosphate buffer (pH 7) with a frequency range from 1×10^6 to 1×10^3 Hz and E_{ac} = 10 mV at open circuit potential.

The 1700 mV reduction of overpotential suggested the efficient electrocatalytic activity of the AuNPs/GO/PEDOT:PSS-modified GCE towards hydrazine oxidation. This is due to the existence of highly conductive AuNPs on the surface of GO/PEDOT:PSS, which reflects faster electron transfer resulting in a more defined and sharper peak for the current of hydrazine oxidation. In addition, it was revealed that the peak current intensity of hydrazine oxidation at the AuNPs/GO/PEDOT:PSS-modified GCE is approximately 11 times higher than that at the GO/PEDOT:PSS-modified GCE. Furthermore, it was also deduced that the higher catalytic activity of hydrazine oxidation is a result of the synergy between AuNPs and the GO/

PEDOT:PSS composite on the GCE surface. Thus, it is expected that this platform based on AuNPs deposited on the GO/PEDOT:PSS-modified GCE will provide a higher sensitivity than the other electrodes for hydrazine detection.

At acidic to neutral pHs of the aqueous solution, hydrazine exists in its protonated state, $N_2H_5^+$ or hydrazinium cation, while at pHs higher than 9.7, N_2H_4 or hydrazine is the predominant species.(50) Since in this work the hydrazine measurement was adjusted to a neutral condition using phosphate buffer (pH 7), we can expect the hydrazinium cation ($N_2H_5^+$) to be the main species in aqueous media. There are two possible mechanisms to explain the interaction between $N_2H_5^+$ and the AuNPs electrodeposited on the GO/PEDOT:PSS composite on the surface of the GCE as shown in Fig. 5(b). First, the electrostatic interaction between sulfonic acid groups (SO_3^- H^+) from the polymeric structure of PSS in the PEDOT:PSS structure with $N_2H_5^+$ (hydrazine form in acidic condition) occurs to form a complex of ($-SO_3^-$ $N_2H_5^+$).(51) Second, the presence of AuNPs on the GO/PEDOT:PSS composite helps to bring $N_2H_5^+$ closer to the electrode surface by the bonding formation between metallic gold and hydrazine via covalent coordination chemistry.(52) Consequently, it can be inferred that the synergy between AuNPs and GO/PEDOT:PSS resulted in a stronger electrocatalytic activity in the hydrazine oxidation on the surface of the modified electrode.

Figure 5(c) shows the cyclic voltammograms at a scan rate of 100 mV s^{-1} from the measurement of 1 mM $K_3[Fe(CN)_6]$ in 0.1 M phosphate buffer (pH 7) using the bare, GO/PEDOT:PSS-modified, and AuNPs/GO/PEDOT:PSS-modified GCEs. From this figure, it can be seen that AuNPs/GO/PEDOT:PSS on the GCE showed the highest oxidation peak (I_{pa} = 28.32 μA) and the highest reduction peak (I_{pc} = 28.27 μA) compared with the other electrodes. Then, the effective surface area from each electrode can be calculated using the Randles–Sevcik equation:

$$i_p = \left(2687 \times 10^5\right) n^{3/2} v^{1/2} A D^{1/2} C, \tag{4}$$

where i_p is the oxidation peak current of $K_3[Fe(CN)_6]$ (Ampere), n is the number of electrons involved in the redox reaction from $[Fe(CN)_6]^{3-}$ to $[Fe(CN)_6]^{4-}$, which is equal to 1, D is the diffusion coefficient of $K_3[Fe(CN)_6]$ (6.70×10^{-6} cm^2 s^{-1}) as reported in Ref. 51, A is the effective surface area of the electrode (cm^2), v is the scan rate (V s^{-1}), and C is the concentration of $[Fe(CN)_6]^{3-}$ (mol cm^{-3}). According to this equation, the effective surface areas for the bare, GO/PEDOT:PSS-modified, and AuNPs/GO/PEDOT:PSS-modified GCEs can be calculated as 0.006, 0.06, and 0.086 cm^2, respectively. It can be deduced from these results that the effective surface area of the AuNPs/GO/PEDOT:PSS-modified GCE was approximately 14 times larger than that of the bare GCE. The increase in effective surface area from this modified electrode could be attributed to the existence of AuNPs on the GO/PEDOT:PSS composite, which works synergistically and thus effectively improves its electrochemical performance for hydrazine oxidation. The synergistic activities from these electrode modifiers could be explained by AuNPs as an electron transfer channel in the electrooxidation of hydrazine, whereas the GO/PEDOT:PSS composite creates a suitable microenvironment for its electrocatalysis.

In accordance with CV studies, EIS was also performed on modified electrodes to study the electron transfer resistance at the electrode interface with respect to their electrochemical activity. Figure 5(d) shows the Nyquist plot obtained from the bare, GO/PEDOT:PSS-modified, and AuNPs/GO/PEDOT:PSS-modified GCEs for the measurement of 1 mM $K_3[Fe(CN)_6]$ in 0.1 M KCl with a frequency range from 10^3 to 5 kHz and E_{ac} = 10 mV at open circuit potential. Figure 5(d) (inset) also shows the equivalent circuit of the fitted Nyquist plot from three modified electrodes, which contains the information about the solution resistance (R_1), charge transfer resistance (R_2), and double-layer capacitance (C_1). In general, R_2 increases when the diameter of a semicircle of the Nyquist plot obtained from the experiments is larger, which represents the low conductivity of the electrode.(53) On the basis of this figure, R_2 can be calculated as 334, 241, and 95 Ω for the bare, GO/PEDOT:PSS-modified, and AuNPs/GO/PEDOT:PSS-modified GCEs, respectively. From these results, it can be inferred that the AuNPs/GO/PEDOT:PSS-modified GCE shows the highest electronic conductivity among the other electrodes, which can be associated with the following two important points: First, the synergistic effects occur between GO and PEDOT:PSS, which increases the electron transport and effective surface area of the modified electrode, and enhances the electrooxidation process for hydrazine.(54,55) Second, the presence of AuNPs on the surface of the GO/PEDOT:PSS composite increases the number of active sites for electron transfer channels and ultimately allows the easy access of reactant molecules to the surfaces of the modified electrodes.(56,57)

3.4 Evaluation of scan rate effect towards hydrazine measurements using AuNPs/GO/PEDOT:PSS-modified GCE

The effect of scan rate on hydrazine oxidation was evaluated using the AuNPs/GO/PEDOT:PSS-modified GCE by measuring 50 μM hydrazine in 0.1 M phosphate buffer (pH 7) at a scan rate of 25 to 150 mV s^{-1}. Figure 6(a) shows the increasing peak current of hydrazine oxidation when the scan rate varied from 25 to 150 mV s^{-1}. From this result, the corresponding linear regression of I_{pa} vs $v^{1/2}$ can be calculated as $I_{pa} = 13.982x - 45.231$; $R^2 = 0.9943$ as shown in Fig. 6(a) (inset). Thus, it can be concluded that the oxidation of hydrazine on the surface of the AuNPs/GO/PEDOT:PSS-modified GCE is controlled by diffusion phenomena and is consistent with previous reports.(58,59) In addition, this type of diffusion-controlled process is very useful for the quantitative detection of hydrazine using the modified electrodes. It can also be observed in this figure that the anodic peak of hydrazine slightly shifts towards a more positive potential with increasing scan rate, which explains that hydrazine oxidation follows the irreversible process in the AuNPs/GO/PEDOT:PSS-modified GCE.

Next, the detailed reaction mechanism determined by the electron transfer coefficient (α) and the number of electrons (n) that participate in the hydrazine oxidation process can be obtained using several systematic calculations. Figure 6(b) shows the linear relationship between the E_p of hydrazine oxidation with the logarithm of scan rates (Tafel plot). On the basis of this figure, the linear equation can be obtained as $y = 172.67x - 105.38$ ($R^2 = 0.9932$). According to the Tafel equation [Eq. (5)], the electron transfer coefficient (α) can be determined using the Tafel slope of the straight line of the linear regression.

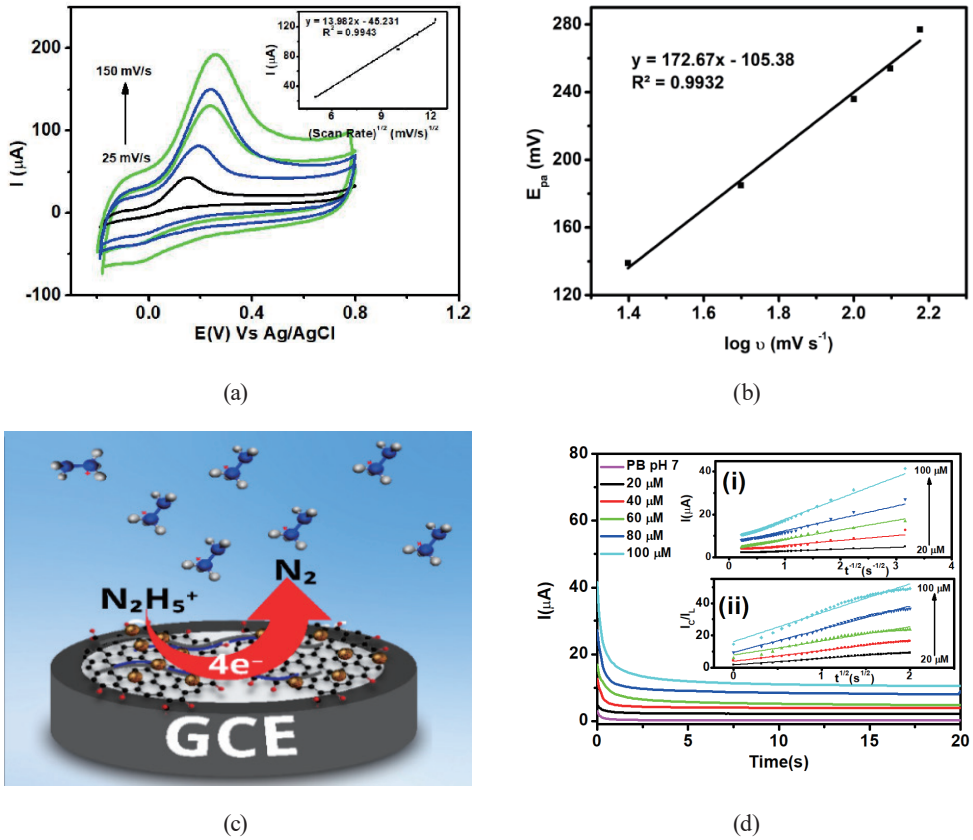

Fig. 6. (Color online) (a) Voltammograms of 50 μM hydrazine in 0.1 M phosphate buffer (PB) (pH 7) with different scan rates (25, 50, 100, 125, and 150 mV s^{-1}). Inset: linear relationship between square root of scan rate versus oxidation current of hydrazine measured with AuNPs/GO/PEDOT:PSS-modified GCE, (b) plot linear as a function of logarithm of scan rate (v) versus peak potential of hydrazine oxidation, (c) schematic illustration of the mechanism of hydrazine oxidation on the surface of AuNPs/GO/PEDOT:PSS-modified GCE, (d) chronoamperometric curves of hydrazine (20−100 μM) in 0.1 M phosphate buffer (pH 7) with an applied potential (E_{dc}) of 0.32 V (vs Ag/AgCl), (i) Cottrell plot for the data from the chronoamperogram, and (ii) dependence of I_C/I_L on $t^{1/2}$ derived from the chronoamperogram data.

$$E_p = \left[2.303RT/(1-\alpha)nF\right]\log v + \text{constant} \tag{5}$$

Here, R is the gas constant (8.314 J K^{-1} mol^{-1}), T is the absolute room temperature (298 K), F is Faraday's constant (96485 C mol^{-1}), and n is the number of electrons that participate in hydrazine oxidation. From the straight line of the Tafel plot [Fig. 6(b)], the Tafel slope can be determined as 173 mV $decade^{-1}$, which suggests that a single electron transfer was involved in the rate-determining step of the hydrazine oxidation process.[60] This result is consistent with several previous reports utilizing various modified electrodes.[61,62]

Moreover, the total number of electrons (n) that participate in the electrochemical reaction of hydrazine oxidation can be estimated from the slope of I_{pa} vs $v^{1/2}$ as shown in Fig. 6(a) (inset). The Randles–Sevcik equation was then employed for the calculation of this irreversible reaction,

which is kinetically controlled by diffusion phenomena at the modified electrodes[63] as shown in Eq. (6).

$$I_p = \left(3.01\times10^5\right)n\left[\left(1-\alpha\right)n_\alpha\right]^{1/2} C_0 A D_0^{1/2} v^{1/2} \tag{6}$$

Here, A is the effective surface area of the electrode (0.086 cm^2), C_0 is the bulk concentration of hydrazine (5×10^{-8} mol cm^{-3}), and D is the diffusion coefficient (2.25×10^{-5} cm^2 s^{-1}). Therefore, the number of electrons (n) transferred in the reaction of hydrazine oxidation can be calculated as $3.56 \approx 4$ according to Fig. 6(a) (inset). On the basis of previous studies,[64,65] the possible mechanism for hydrazine oxidation on the surface of the AuNPs/GO/PEDOT:PSS-modified GCE can be illustrated by the following equations:[66]

$$N_2H_5^+ + H_2O \leftrightarrow N_2H_4 + H_3O^+, \tag{7}$$

$$N_2H_4 + H_2O \rightarrow N_2H_4^{\bullet+} + H_3O^+ + e^-, \tag{8}$$

$$N_2H_4^{\bullet+} + 3H_2O \rightarrow N_2 + 3H_3O^+ + 3e^-. \tag{9}$$

From these equations, it can be deduced that hydrazine oxidation occurs with a single electron transfer in a rate-determining step (8), followed by a rapid three-electron transfer process (9). Thus, the overall reaction of hydrazine oxidation can be defined as shown in Fig. 6(c) and following the equation

$$N_2H_5^+ + 4H_2O \rightarrow N_2 + 4H_3O^+ + 4e^-. \tag{10}$$

Next, the diffusion coefficient (D) and catalytic rate constant (k) of hydrazine measurements at the AuNPs/GO/PEDOT:PSS-modified GCE can be determined using the chronoamperometry technique. Figure 6(d) shows a chronoamperogram obtained from different concentrations of hydrazine (20–100 μM) at an applied potential of 0.32 V (vs Ag/AgCl). Then, the diffusion coefficient of hydrazine measurements can be determined using the following Cottrell equation:[67]

$$I_p = nFACD^{1/2}/\pi^{1/2}t^{1/2}, \tag{11}$$

where I_p is the oxidation current of hydrazine measured with the AuNPs/GO/PEDOT:PSS-modified GCE, A is the surface area of the electrode (cm^2), F is Faraday's constant, C is the hydrazine concentration (1×10^{-7} mol cm^{-3}), D is the diffusion coefficient (cm^2 s^{-1}), and t is time (s). Then, D can be calculated as 2.25×10^{-5} cm^2 s^{-1} on the basis of the provided linear regression in Fig. 6(d)(i) (inset). In addition, the rate constant (k) for the electrocatalytic oxidation of hydrazine by the AuNPs/GO/PEDOT:PSS-modified GCE can be calculated as[68]

$$I_c / I_L = \left(\pi k C_o t\right)^{1/2}, \tag{12}$$

where I_c is the catalytic current of hydrazine measured with the AuNPs/GO/PEDOT:PSS-modified GCE, I_L is the finite current without hydrazine, k is the catalytic rate constant (cm^3 mol^{-1} s^{-1}), C_o is the hydrazine concentration (mol cm^{-3}), and t is time (s). On the basis of the slope of I_c/I_L vs $t^{1/2}$ in Fig. 6(d)(ii) (inset), k is found to be 1.03×10^{-6} cm^3 mol^{-1} s^{-1}. This result shows that the AuNPs/GO/PEDOT:PSS-modified GCE provides good electrocatalytic activity for hydrazine oxidation. In addition, this electrode based on a combination of AuNPs with a material composite consisting of carbon and conductive polymer revealed a promising platform for the investigation of the electrocatalytic process of quantitative hydrazine determination.

3.5 Analytical performance of AuNPs/GO/PEDOT:PSS/GCE for hydrazine detection

The amperometric technique is one of the most appropriate and rapid methods for the detection of low-concentration analytes either in a synthetic or sample solution. Thus, we used this technique for hydrazine determination to achieve a higher sensitivity and a lower detection limit using the AuNPs/GO/PEDOT:PSS-modified GCE. Figure 7(a) shows the chronoamperogram recorded from the measurements of various concentrations of hydrazine (0.2–100 μM) in 0.1 M phosphate buffer (pH 7) at a potential of 0.32 V under continuous stirring conditions. The applied potential of 0.32 V was selected owing to its optimum current response, thus giving the highest sensitivity based on Fig. 5(a). Then, the resulting chronoamperogram in Fig. 7(a) illustrates the rapid and sensitive detection of hydrazine using the modified electrode with oxidation peak current increasing linearly with the concentration of hydrazine. It can also be seen from the assessment of the chronoamperometric studies of hydrazine measurements in this figure that there are two obtained corresponding calibration plots in two different ranges of hydrazine concentrations. The corresponding linear equations are I_p (μA) = $0.5798C_{hydrazine}$ + 0.5046 (R^2 = 0.9907, 0.2–1.0 μM) and I_p (μA) = $0.1271C_{hydrazine}$ + 0.5981 (R^2 = 0.9935, 10–100 μM) [Fig. 7(b)]. In addition, the sensitivities from these two linear equations can be calculated as 0.598 μA μM^{-1} (0.2–1.0 μM) and 0.127 μA μM^{-1} (10–100 μM). Furthermore, the LOD and LOQ can be obtained as 0.005 μM (1.6×10^{-4} μg mL^{-1}) and 0.08 μM (2.56×10^{-3} μg mL^{-1}), respectively. According to EPA regulations, the LOD derived from this experiment was lower than the permissible threshold limit of 0.312 μM (10 ppb).[69] Therefore, it can be concluded that this proposed sensor has high sensitivity for hydrazine detection with prospective application to be employed in real samples.

The different electrode modifiers employed for the electrochemical detection of hydrazine are shown in Table 1, where the proposed sensor exhibits an analytical performance comparable to those of previous sensors. From Table 1, it is evident that the proposed sensor offers a higher sensitivity and a wider analytical range for hydrazine detection than other sensors,[70–72,74,76–78] although several previous hydrazine sensors still exhibited superior analytical performance in terms of wider analytical range, lower LOD, and higher sensitivity.[73,75,79–81] However, this developed method offers a simple approach to modifying the electrode surface by using an

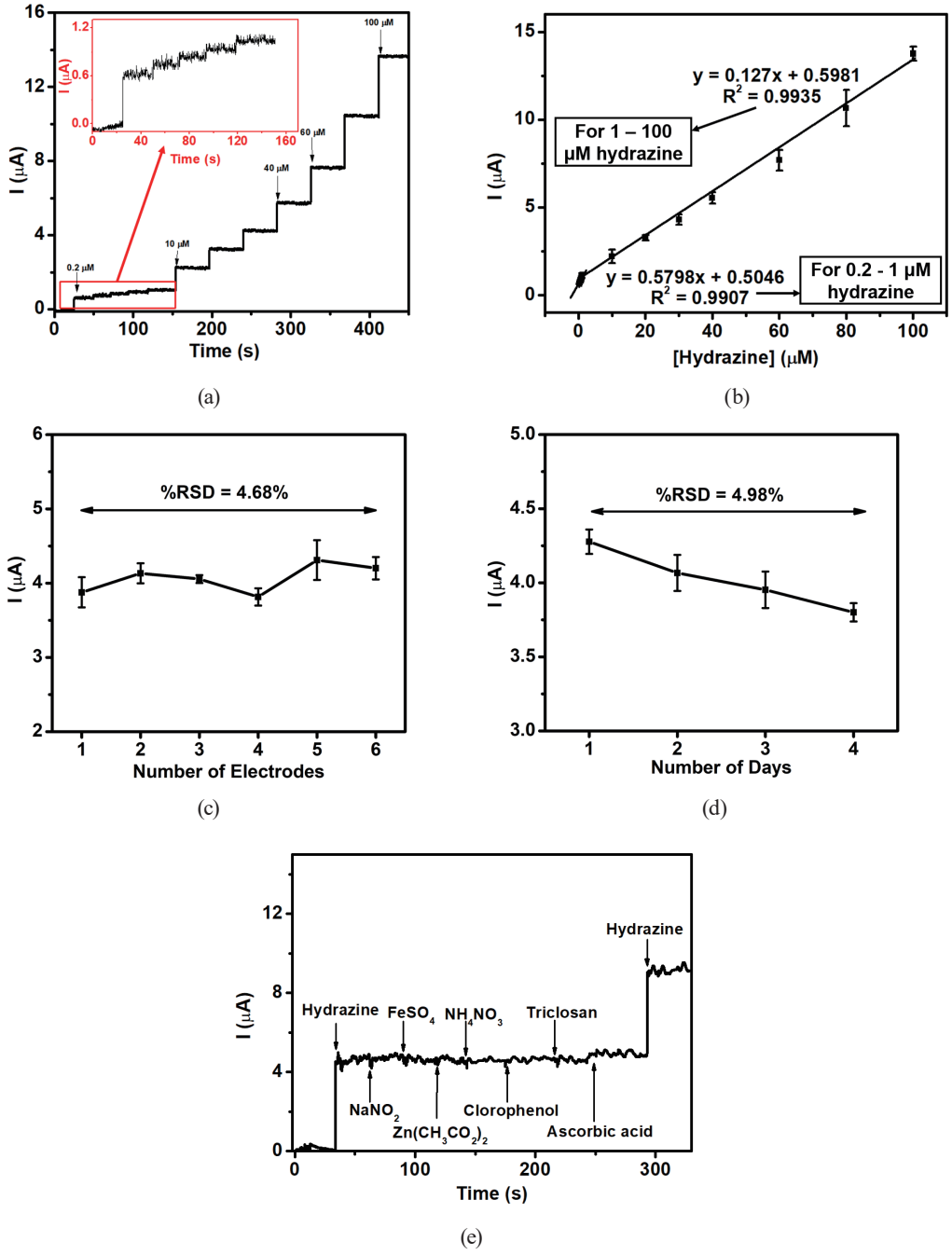

(a) (b) (c) (d) (e)

Fig. 7. (Color online) (a) Chronoamperometric response obtained from consecutive additions (0.2–100 μM) of hydrazine using AuNPs/GO/PEDOT:PSS-modified GCE, (b) the corresponding calibration curve of the current response of hydrazine oxidation versus its concentration in two different ranges, (c) reproducibility of five different AuNPs/GO/PEDOT:PSS-modified GCEs for the measurement of 30 μM hydrazine in 0.1 M PB (pH 7), (d) stability measurements in four consecutive days of the proposed sensor using 0.1 M PB (pH 7) containing 30 μM hydrazine, and (e) chronoamperogram of 30 μM hydrazine in 0.1 M PB (pH 7) with addition of several interferences at each concentration of 30 μM [$NaNO_2$, $FeSO_4$, $Zn(CH_3CO_2)_2$, NH_4NO_3, chlorophenol, triclosan, and ascorbic acid].

Table 1
Comparison of AuNPs/GO/PEDOT:PSS/GCE with other modified electrodes for hydrazine detection.

Electrode	Linear range (μM)	LOD (μM)	Sensitivity ($\mu A\ mM^{-1}\ cm^{-2}$)	Ref.
ErGO[a]/PEDOT:PSS	0.2–100; 1–100 μM	0.01	196.7; 24.7	(30)
CoS_2/HNGC[b]	1 μM–3 mM	0.272	2384	(72)
rGO/MoS_2/Au electrode	0.1–1.0 μM	0.132	89.9	(73)
Ag/PPTI[c]	0.05–50 μM	0.05	0.45	(74)
MoS_2-QDs@Fe_3O_4/rGO	0.8–2190 μM	0.12	0.0353	(75)
NiCo-LDHs@h-Ni NWS	10 μM–8 mM	0.29	312.8	(76)
Co_3S_4/Ti Mesh	0.005–2 mM	0.7	2956	(77)
Cu_2L_2[d]	0.5–27 μM	0.5	0.603	(78)
CoS_2@NC/CNTs[e]	1.0 μM–6.0 mM	0.096	2101	(79)
NiCo-LDH	0.001–1 mM; 1–7 mM	0.043	5342; 2965	(80)
NiO nanoflower	0.99–98.13 μM	0.026	547	(81)
Au@CNO[f]	0.05–1000 μM	0.012	485.7	(82)
Co(OH)F@NiMn-LDH NSA/CC	2 μM–7 mM	0.21	2850	(83)
AuNPs/GO/PEDOT:PSS	0.2–1; 1–100 μM	0.005	579.8; 127	This work

[a]Electrochemically reduced graphene oxide. [b]N-doped mesoporous graphite carbon nanocages. [c]Polyperylene-tetraamide. [d]Copper thiosemicarbazone. [e]3D hexagonal star-like carbon nanotube. [f]Carbon nano-onions.

electrodeposition technique to enhance sensitivity for hydrazine detection. In addition, the synergy activities between AuNPs with GO/PEDOT:PSS result in the high conductivity of the material composite and could enhance the signal amplification due to a faster electron transfer at the surfaces of the modified electrodes. Therefore, from the above discussion, it can be concluded that the proposed hydrazine sensor based on the AuNPs/GO/PEDOT:PSS-modified GCE demonstrates its potential to be employed in hydrazine sensing for practical applications.

3.6 Evaluation of reproducibility, stability, and selectivity of AuNPs/GO/PEDOT:PSS-modified GCE

The sensor reproducibility and stability of the AuNPs/GO/PEDOT:PSS-modified GCE were evaluated in a solution of 0.1 M phosphate buffer (pH 7) containing 30 μM hydrazine using the amperometric technique. Sensor reproducibility was evaluated by measuring six different AuNPs/GO/PEDOT:PSS-modified GCEs for 30 μM hydrazine under similar experimental conditions. Sensor stability was evaluated by using a single AuNPs/GO/PEDOT:PSS-modified GCE for the measurements of 30 μM hydrazine for four consecutive days. Relative standard deviations (RSDs) of 4.68% for sensor reproducibility [Fig. 7(c)] and 4.98% for sensor stability [Fig. 7(d)] were obtained. All measurements for the evaluation of sensor reproducibility and stability were performed in triplicates. Therefore, it can be inferred that the proposed sensor based on the AuNPs/GO/PEDOT:PSS-modified GCE displays good and reliable analytical performance to be used further in the analysis of real samples, such as tap and drinking water.

The selectivity of the proposed sensor was then employed to investigate the interference effects of various interfering species [$NaNO_2$, $FeSO_4$, $Zn(CH_3CO_2)_2$, NH_4NO_3, chlorophenol, triclosan, and ascorbic acid], which may be present in real samples. Figure 7(e) shows the

chronoamperometric response from the measurements of 30 μM hydrazine in the presence of several interfering species in the concentration ratio of 1:1. From this figure, it is clear that the addition of these potential interfering species has a negligible effect on the oxidation current of hydrazine. More importantly, when hydrazine was introduced again to the solution containing all the potential interfering species, the oxidation current of hydrazine increases again. This result indicates that the proposed sensor has good selectivity towards hydrazine detection using the AuNPs/GO/PEDOT:PSS-modified GCE. In addition, this result was then quantitatively analyzed to obtain the relative standard deviation (RSD) and was in the acceptable range (93–104%) as summarized in Table 2. Therefore, the data summarized in this table confirm that the AuNPs/GO/PEDOT:PSS-modified GCE has a promising potency to be used for hydrazine detection in real samples.

3.7 Comparison of hydrazine detection in real samples using the proposed sensor (AuNPs/GO/PEDOT:PSS-modified GCE) with standard spectrophotometric technique

To determine whether this sensor could be used in real sample analysis for hydrazine detection, two experiments were performed using two samples of water obtained from different sources, tap and drinking water. Both water samples were analyzed using the proposed sensor (AuNPs/GO/PEDOT:PSS-modified GCE) using the amperometry technique, which was compared with the standard spectrophotometric method to evaluate its accuracy. Hydrazine was added at different concentrations to the water samples using the standard addition method to obtain its recovery and RSD. All data from the hydrazine determination in tap and drinking water were obtained in triplicate experiments by electrochemical and spectrophotometric techniques. As shown in Table 3, the recovery values for tap and drinking water are in the acceptable analytical range for both electrochemical (98–102%) and spectrophotometric (98–104%) techniques. In addition, the RSDs for both techniques are also in the acceptable range with %RSD less than 5%. The recovery values from both techniques were further statistically analyzed using Student's *t*-test at the 95% confidence interval. It was obtained from Student's *t*-test that there is no significant difference between these two techniques, suggesting that this proposed sensor can be potentially employed for the assessment of water quality in the environment, particularly for hydrazine sensing.

Table 2
Interference effect and recovery value of hydrazine measurement at 30 μM concentration.

Interferences	Interference:HZ	IHZ (μA)	Recovery (%)
—	—	4.3 ± 0.3	—
$NaNO_2$	1:1	4.1 ± 0.2	94.6
$FeSO_4$	1:1	4.3 ± 0.3	99.0
$Zn(CH_3CO_2)_2$	1:1	4.0 ± 0.2	93.1
NH_4NO_3	1:1	4.0 ± 0.1	94.2
Chlorophenol	1:1	4.1 ± 0.0	94.8
Triclosan	1:1	4.0 ± 0.1	92.6
Ascorbic acid	1:1	4.5 ± 0.1	104.3

Table 3
Comparison of results of hydrazine detection in real samples (tap and drinking water) using the proposed sensor and standard spectrophotometric technique.

Sample	Added (μM)	Electrochemical			Spectrophotometry		
		Found (μM)	Recovery (%)	RSD (%)	Found (μM)	Recovery (%)	RSD (%)
Tap water	0.2	0.20	101.14	3.96	0.20	100.11	2.07
	0.5	0.51	101.45	3.56	0.50	99.23	2.77
	0.8	0.80	100.25	4.05	0.81	101.25	1.94
	10	9.85	98.52	4.04	10.20	102.23	4.85
	40	40.97	102.43	3.63	40.90	100.47	3.69
	60	60.85	101.42	4.05	60.61	101.01	1.77
Drinking water	0.2	0.20	100.02	4.86	0.20	98.25	4.90
	0.5	0.50	99.26	4.80	0.50	100.29	2.40
	0.8	0.80	99.42	4.93	0.79	98.60	4.93
	10	10.01	100.10	3.69	10.49	104.88	2.79
	40	39.87	99.68	4.76	40.72	101.80	1.89
	60	60.13	100.22	2.20	59.94	99.91	2.67

4. Conclusion

We have demonstrated the successful fabrication of an amperometric hydrazine sensor based on AuNPs electrodeposited on the composite of the GO/PEDOT:PSS-modified GCE. We found that the optimum experimental condition for AuNP electrodeposition on the GO/PEDOT:PSS composite is 15 cycles of electrodeposition at a scan rate of 100 mV s^{-1}. The electrode modifier consisting of AuNPs on the GO/PEDOT:PSS composite was then characterized using several instrumentation techniques such as Raman, FTIR, XRD, SEM-EDS, AFM, and EIS. The amperometric hydrazine sensor exhibited excellent electrocatalytic activity compared with the bare and GO/PEDOT:PSS-modified GCEs. This enhanced electrocatalytic activity of hydrazine oxidation is attributed to the synergistic effect between AuNPs as the electron transfer channel and the GO/PEDOT:PSS composite as the highly conductive material, which can increase the electrode conductivity. In terms of its analytical performance, the fabricated amperometric hydrazine sensor also demonstrated a linear response for hydrazine detection from 0.2 to 100 μM with a low LOD of 0.005 μM (S/N = 3) and good sensitivity of 579.8 μA mM^{-1} cm^{-2}. In addition, this proposed amperometric hydrazine sensor shows acceptable reproducibility, stability, and selectivity towards several potential interfering species that might be present in environmental water. This proposed sensor has been tested in two different types of water, namely, tap and drinking water, for hydrazine detection, and the results showed no significant difference with the standard spectrophotometric technique. Thus, this work demonstrated a promising potency of the amperometric sensor based on AuNPs electrodeposited on the GO/PEDOT:PSS composite-modified GCE for the highly sensitive detection of hydrazine with a low LOD.

Acknowledgments

We would like to acknowledge The Directorate General of Higher Education, Research, and Technology, Ministry of Education, Culture, Research and Technology, Republic of Indonesia for the research funding in scheme Penelitian Tesis Magister fiscal year 2023 with contract No. 102/E5/PG.02.00.PL/2023.

References

1 R. Jimenez-Perez, J. Agrisuelas, A. Gomis-Berenguer, M. T. Baeza-Romero, and E. Valero: Electrochim. Acta **461** (2023) 142683. https://doi.org/10.1016/j.electacta.2023.142683
2 N. T. Dat, N. N. Tien, N. T. T. Ngan, and V. T. Thu: Analyst **148** (2023) 1777. https://doi.org/10.1039/D3AN00110E
3 X. Mamat, H. A. Aisa, and L. Chen: Nanomaterials **13** (2023) 1571. https://doi.org/10.3390/nano13091571
4 M. Sethupathi, B. Thulasinathan, M. Jayaraman, P. Manickam, and N. Rajasekaran: ECS J. Solid State Sci. Technol. **12** (2023) 067003. https://doi.org/10.1149/2162-8777/acda60
5 Adiraju, R. Munjal, C. Viehweger, A. Al-Hamry, A. Brahem, J. Hussain, S. Kommisetty, A. Jalasutram, C. Tegenkamp, and O. Kanoun: Sensors **23** (2023) 2961. https://doi.org/10.3390/s23062961
6 S. Madhu, J. H. Han, C. W. Jeong, and J. Choi: Anal. Chim. Acta **1238** (2023) 340644. https://doi.org/10.1016/j.aca.2022.340644
7 A. Berni, A. Amine, J. J. Garcia-Guzman, L. Cubillana-Aguilera, and J. M. Palacios-Santander: Biosensors **13** (2023) 678. https://doi.org/10.3390/bios13070678
8 N. Malarat, W. Oin, K. Kanjana, F. Makkliang, M. Siaj, and S. Poorahong: Microchem. J. **188** (2023) 108473. https://doi.org/10.1016/j.microc.2023.108473
9 K. Okamoto, H. Kawakami, Y.-A. Chien, T. Kurioka, W.-T. Chiu, P. Chakraborty, T. Nakamoto, Y.-Y. Hsu, M. Sone, and T.-F. M. Chang: MNE **18** (2023) 100175. https://doi.org/10.1016/j.mne.2023.100175
10 Q. Luo, Y. Su, and H. Zhang: J. Iran. Chem. Soc. **20** (2023) 731. https://doi.org/10.1007/s13738-022-02711-8
11 X. Chai, S. Ye, F. Wang, H. Yuan, M. Liu, F. Fan, L. Zhang, X. Zhang, T. Wang, and Y. Fu: Inorg. Chem. **62** (2023) 10694. https://doi.org/10.1021/acs.inorgchem.3c01148
12 A. Urcuk, C. Yildiz, D. E. Bayraktepe, and Z. Yazan: Microchem. J. **193** (2023) 109079. https://doi.org/10.1016/j.microc.2023.109079
13 D. S. Sipuka, O. A. Arotiba, T. I. Sebokolodi, T. R. Tsekeli, and D. Nkosi: Electroanalysis **35** (2023) e202200099. https://doi.org/10.1002/elan.202200099
14 Y. Wu, T. Zhang, L. Shu, and X. Wu: Biosensors **13** (2023) 563. https://doi.org/10.3390/bios13050563
15 I. Kocak: J. Pharm. Biomed. Anal. **234** (2023) 115518. https://doi.org/10.1016/j.jpba.2023.115518
16 M. A. Kamyabi, S. Jadali, L. S. Khangheslaghi, and M. K. H. Heris: New J. Chem. **47** (2023) 1209. https://doi.org/10.1039/D2NJ05164H
17 F. Zhou and C. Sun: Inorg. Chem. Front. **10** (2023) 3058. https://doi.org/10.1039/D3QI00568B
18 L. Hu, J. Wang, H. Wang, Y. Zhang, and J. Han: ACS Appl. Mater. Interfaces **15** (2023) 15449. https://doi.org/10.1021/acsami.2c22423
19 P. Morales-Gil, M. G. M. de Oca-Yemha, F. Perez-Cruz, M. Romero-Romo, M. T. Ramirez-Silva, J. Aldana-Gonzalez, and M. P. Pardave: J. Mol. Liq. **386** (2023) 122499. https://doi.org/10.1016/j.molliq.2023.122499
20 T. M. Day, P. R. Unwin, and J. V. Macpherson: Nano Lett. **7** (2007) 51. https://doi.org/10.1021/nl061974d
21 B. R. Putra, U. Nisa, R. Heryanto, E. Rohaeti, M. Khalil, A. Izzataddini, and W. T. Wahyuni: Anal. Sci. **38** (2022) 157. https://doi.org/10.2116/analsci.21P214
22 W. Anindya, W. T. Wahyuni, M. Rafi, and B. R. Putra: Int. J. Electrochem. Sci. **18** (2023) 100034. https://doi.org/10.1016/j.ijoes.2023.100034
23 S. A. H. Ta'alia, E. Rohaeti, B. R. Putra, and W. T. Wahyuni: Results Chem. **6** (2023) 101024. https://doi.org/10.1016/j.rechem.2023.101024
24 G. Greco, A. Giuri, S. Bagheri, M. Seiti, O. Degryse, A. Rizzo, C. Mele, E. Ferraris, and C. E. Corcione: Molecules **28** (2023) 2963. https://doi.org/10.3390/molecules28072963
25 M. M. Dehbali, M. Farahmandpour, S. Hamedi, and Z. Kordrostami: Sci. Reports **13** (2023) 9505. https://doi.org/10.1038/s41598-023-36612-4
26 P. H. S. Borges, L. C. D. Narciso, G. F. S. Miguel, G. S. Oliveira, M. C. Junior, A. E. H. Machado, R. A. A. Munoz, and E. Nossol: Electrochim. Acta **445** (2023) 142018. https://doi.org/10.1016/j.electacta.2023.142018

27 Ahmad and H. Kim: Mater. Chem. Phys. **296** (2023) 127260. https://doi.org/10.1016/j.matchemphys.2022.127260
28 M. Singh, S. R. Bhardiya, A. Rai, V. K. Rai: Curr. Anal. Chem. **19** (2023) 27. https://doi.org/10.2174/1573411018666220421104413
29 K. Yan, L.Yan, W. Kang, A. Kaffash, B. Mahdavi, M. Baghayeri, W. Liu: Environ. Res. **238** (2023) 117081. https://doi.org/10.1016/j.envres.2023.117081
30 H. A. Rahman, M. Rafi, B. R. Putra, and W. T. Wahyuni: ACS Omega **8** (2023) 3258. https://doi.org/10.1021/acsomega.2c06791
31 R. D. Crapnell and C. E. Banks: Sens. Diagn. **1** (2022) 71. https://doi.org/10.1039/D1SD00006C
32 Z. Zhao, Y. Sun, P. Li, W. Zhang, K. Lian, J. Hu, and Y. Chen: Talanta **158** (2016) 283. https://doi.org/10.1016/j.talanta.2016.05.065
33 S. Claramunt, A. Varea, D. Lopez-Diaz, M. M. Velazquez, A. Cornet, and A. Cirera: J. Phys. Chem. C **119** (2015) 10123. https://doi.org/10.1021/acs.jpcc.5b01590
34 V. Agarwal and P. B. Zetterlund: Chem. Eng. J. **405** (2021) 127018. https://doi.org/10.1016/j.cej.2020.127018
35 A. Kaniyoor and S. Ramaprabhu: AIP Adv. **2** (2012) 032183. https://doi.org/10.1063/1.4756995
36 S. Xiong, L. Zhang, and X. Lu: Polym. Bull. **70** (2013) 237. https://doi.org/10.1007/s00289-012-0833-8
37 D. Antiohos, M. S. Romano, J. M. Razal, S. Beirne, P. Aitchison, A. I. Minett, G. G. Wallace, and J. Chen: J. Mater. Chem. A **2** (2014) 14835. https://doi.org/10.1039/c4ta02190h
38 X. Zhang, D. Chang, J. Liu, and Y. Luo: J. Mater. Chem. **20** (2010) 5080. https://doi.org/10.1039/C0JM00050G
39 Li, J. Liu, C. Gao, J. Zhang, and H. Sun: Int. J. Photoenergy **2009** (2009) Article ID 650509. https://doi.org/10.1155/2009/650509
40 Zhang, L. L. Zhang, X. S. Zhao, and J. Wu: Chem. Mater. **22** (2010) 1392. https://doi.org/10.1021/cm902876u
41 F. Abd-Wahab, H. F. A. Guthoos, and W. W. A. W. Salim: Biosensors **9** (2019) 36. https://doi.org/10.3390/bios9010036
42 T. Beduk, E. Bihar, S. G. Surya, A. N. Castillo, S. Inal, and K. N. Salama: Sens. Actuators, B **306** (2020) 127539. https://doi.org/10.1016/j.snb.2019.127539
43 G. Gotti, K. Fajerwerg, D. Evrard, and P. Gros: Electrochim. Acta **128** (2014) 412. https://doi.org/10.1016/j.electacta.2013.10.172.
44 T. Hezard, K. Fajerwerg, D. Evrard, V. Colliere, P. Behra, and P. Gros: J. Electroanal. Chem. **664** (2012) 46. https://doi.org/10.1016/j.jelechem.2011.10.014
45 T. G. S. Babu, D. Varadarajan, G. Murugan, T. Ramachandran, and B. G. Nair: J. Appl. Electrochem. **42** (2012) 427. https://doi.org/10.1007/s10800-012-0416-2
46 X. Yiwei, Z. Wen, S. Jiyong, X. Xiaobo, L. Yianxiao, H. E. Thahir, H. Xiaowei, L. Zhihua, Z. Xiaodong, and H. Xuetao: Food Chem. **237** (2017) 423. https://doi.org/10.1016/j.foodchem.2017.05.096
47 K. Jasuja and V. Berry: ACS Nano. **3** (2009) 2358. https://doi.org/10.1021/nn900504v
48 J. Xiao and L. Qi: Nanoscale **3** (2011) 1383. https://doi.org/10.1039/C0NR00814A
49 S. Denidson, P. S. Kumar, A. J. Jeevaghan, T. Adinaveen, P. Muthukumar, and M. Amalraj: Appl. Nanosci. **13** (2023) 5949. https://doi.org/10.1007/s13204-023-02869-4
50 R. A. Escalona-Villalpando, M. P. Gurrola, G. Trejo, M. Guerra-Balcazar, J. Ledesma-Garcia, and L. G. Arriaga: J. Electroanal. Chem. **816** (2018) 92. https://doi.org/10.1016/j.jelechem.2018.03.037
51 R. Miao and R. G. Compton: Electrochim. Acta **388** (2021) 138655. https://doi.org/10.1016/j.electacta.2021.138655
52 H. Park, S. H. Lee, F. S. Kim, H. H. Choi, I. W. Cheong, and J. H. Kim: J. Mater. Chem. A **2** (2014) 6532. https://doi.org/10.1039/c3ta14960a
53 J.-J. Jasmin, F. Miserque, E. Dumas, I. Vickridge, J.-J. Ganem, C. Cannizzo, and A. Chausse: Appl. Surf. Sci. **397** (2017) 159. https://doi.org/10.1016/j.apsusc.2016.11.125
54 J. Feng, G. Lang, T. Li, J. Zhang, J. Zhao, W. Li, W. Yang, and Z. Jiang: Appl. Surf. Sci. **604** (2022) 154548. https://doi.org/10.1016/j.apsusc.2022.154548
55 G. Kaladevi, P. Wilson, and K. Pandian: Ionics **26** (2020) 3123. https://doi.org/10.1007/s11581-020-03457-0
56 G. Greco, A. Giuri, S. Bagheri, M. Seiti, O. Degryse, A. Rizzo, C. Mele, E. Ferraris, and C. E. Corcione: Molecules **28** (2023) 2963. https://doi.org/10.3390/molecules28072963
57 A. Wong, A. M. Santos, O. Fatibello-Filho: J. Electroanal. Chem. **799** (2017) 547. https://doi.org/10.1016/j.jelechem.2017.06.055
58 D. Linh, N. T. T. Huyen, N. H. Dang, B. Piro, and V. T. Thu: RSC Adv. **13** (2023) 10082. https://doi.org/10.1039/D3RA00793F
59 D. S. Sipuka, T. I. Sebokolodi, F. O. G. Olorundare, C. Muzenda, O. V. Nkwachukwu, D. Nkosi, and O. A. Arotiba: Electrocatalysis **14** (2023) 9. https://doi.org/10.1007/s12678-022-00769-9
60 Faisal, F. A. Harraz, A. E. Al-Salami, S. A. Al-Sayari, A. Al-Hajry, and M. S. Al-Assiri: Mater. Chem. Phys. **214** (2018) 126. https://doi.org/10.1016/j.matchemphys.2018.04.085

61 Karuppiah, M. Velmurugan, S.-M. Chen, R. Devasenathipathy, R. Karthik, and S.-F. Wang: Electroanalysis **28** (2015) 808. https://doi.org/10.1002/elan.201500453
62 W. Wang, Z. Zhao, Q. Lei, W. Zhang, P. Li, W. Zhang, S. Zhuiykov, and J. Hu: Appl. Surf. Sci. **542** (2021) 148539. https://doi.org/10.1016/j.apsusc.2020.148539
63 H. M. A. Amin, M. F. El-Kady, N. F. Atta, and A. Galal: Electroanalysis **30** (2018) 1757. https://doi.org/10.1002/elan.201800125
64 J. Li and X. Lin: Sens. Actuators, B **126** (2007) 527. https://doi.org/10.1016/j.snb.2007.03.044
65 Y. Wang, Y. Wan, and D. Zhang: Electrochem. Commun. **12** (2010) 187. https://doi.org/10.1016/j.elecom.2009.11.019
66 R. Gupta, P. K. Rastogi, V. Ganesan, D. K. Yadav, and P. K. Sonkar: Sens. Actuators, B **239** (2017) 970. https://doi.org/10.1016/j.snb.2016.08.117
67 M. Nguyen, L. G. Bach, and Q. B. Bui: J. Pharm. Biomed. Anal. **172** (2019) 243. https://doi.org/10.1016/j.jpba.2019.04.008
68 R. Miao, M. Yang, and R. G. Compton, J. Phys. Chem. Lett. **12** (2021) 6661. https://doi.org/10.1021/acs.jpclett.1c01955
69 F. Amiripour, S. N. Azizi, and S. Ghasemi: Biosens. Bioelectron. **107** (2018) 111. https://doi.org/10.1016/j.bios.2018.02.016
70 S. N. Azizi, S. Ghasemi, and F. Amiripour: Electrochim. Acta **137** (2014) 395. https://doi.org/10.1016/j.electacta.2014.05.158
71 R. D. Crapnell and C. E. Banks: Sens. Diagn. **1** (2022) 71. https://doi.org/10.1039/D1SD00006C
72 J. Yang, S. Zhao, J. Wu, C. Ling, X. Tang, K. Huang, Z. Zou, H. Yu, and X. Xiong: J. Electrochem. Soc. **170** (2023) 047503. https://doi.org/10.1149/1945-7111/acc978
73 S. Rana, S. Kalia, N. Takur, R. K. Singh, R. Kumar, and D. Singh: Mater. Chem. Phys. **294** (2023) 127048. https://doi.org/10.1016/j.matchemphys.2022.127048
74 J. Xu, X. Long, J. Zhang, and S. Wu: Pigment Resin Technol. **52** (2023) 413. https://doi.org/10.1108/PRT-09-2021-0120
75 Lotfi, M. R. Majidi, and K. Asadpour-Zeynali: Synth. Met. **296** (2023) 117361. https://doi.org/10.1016/j.synthmet.2023.117361
76 A. Mahieddine and L. Adnane-Amara: J. Electroanal. Chem. **930** (2023) 117168. https://doi.org/10.1016/j.jelechem.2023.117168
77 J. Wang, R. Li, R. Li, T. Xie, S. Liu, and Y. Wang: New. J. Chem. **43** (2023) 11071. https://doi.org/10.1039/D3NJ01482G
78 M. Thamaraichelvan, A. Sebastian, M. Ganapathi, H. Holla, P. Duraippandi, and N. S. V. Narayanan: Results Chem. **6** (2023) 101025. https://doi.org/10.1016/j.rechem.2023.101025
79 C. Ling, J. Wu, S. Zhao, J. Yang, K. Huang, Z. Zou, H. Yu, J. Ye, and X. Xiong: Coll. Surf. A: Physicochem. Eng. Asp. **672** (2023) 131780. https://doi.org/10.1016/j.colsurfa.2023.131780
80 X. Tang, S. Zhao, J. Wu, Z. He, Y. Zhang, K. Huang, Z. Zou, and X. Xiong: Food Chem. **427** (2023) 136648. https://doi.org/10.1016/j.foodchem.2023.136648
81 R. M. Ferreira, F. M. Morawski, E. C. Pessanha, S. L. S. de Lima, D. S. da Costa, G. A. C. Ribeiro, J. Vaz, R. Mouta, A. A. Tanaka, L. Liu, M. I. P. da Silva, A. Tofanello, H. A. Vitorino, A. G. M. da Silva, and M. A. S. Garcia: ACS Omega **8** (2023) 11978. https://doi.org/10.1021/acsomega.2c07638
82 N. S. K. Gowthaman, D. Mohapatra, P. Arul, and W. S. Chang: J. Ind. Eng. Chem. **117** (2023) 227. https://doi.org/10.1016/j.jiec.2022.10.009
83 S. Zhao, Y. Zhang, J. Eu, C. Ling, Y. Xing, H. Yu, K. Huang, Z. Zou, and X. Xiong: Microchem. J. **185** (2023) 108255. https://doi.org/10.1016/j.microc.2022.108255

About the Authors

Hemas Arif Rahman received his B.S. and M.S. degrees from IPB University, Indonesia, in 2022 and 2023, respectively. He worked on the development of hydrazine sensors for his undergraduate and graduate theses. His research interests are in electrochemical sensors. (hemasrahman@apps.ipb.ac.id)

Budi Riza Putra received his Ph.D. degree from the University of Bath, United Kingdom, in 2020. From 2020 to 2021, he was a lecturer at the Indonesia Defense University, Indonesia. Since 2022, he has been a researcher at the Research Center for Metallurgy, National Research and Innovation Agency, Indonesia. His research interests are in electrochemistry, nanoparticles, and electrochemical sensors. (budi.riza.putra@brin.go.id)

Mohamad Rafi received his Ph.D. degree from Gifu University, Japan, in 2013. From 2006 to 2023, he was an assistant professor at the Department of Chemistry, IPB University, Indonesia, and a professor since 2023. His research interests are in analytical chemistry, chromatography, and metabolomics. (mra@apps.ipb.ac.id)

Rudi Heryanto received his B.S. and M.S. degrees from IPB University, Indonesia, in 1998 and 2005, respectively. From 2006 to 2022, he was an assistant professor at the Department of Chemistry, IPB University, Indonesia, and an associate professor since 2023. His research interests are in analytical chemistry and chemometrics (kemometrik@gmail.com)

Chika Takai-Yamashita received her Ph.D. degree from Nagoya Institute of Technology, Japan, in 2007. From 2007 to 2010, she was a researcher at the Technology Development Headquarters, Kurimoto Ltd., Japan. From 2011 to 2018, she was active as a researcher at Nagoya Institute of Technology. In 2018, she became an assistant professor at the Department of Chemistry and Biomolecular Science, Gifu University, Japan, and an associate professor since 2022. Through the cross-appointment system, she has been an associate professor in Tohoku University since 2023. Her research interests are in nanoparticle synthesis, particle dispersion and structure controls, and particle functionalization. (takai.chika.h3@f.gifu-u.ac.jp)

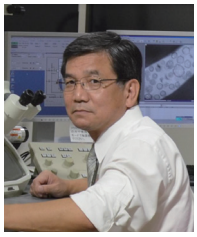

Yutaka Ohya received his Ph.D. degree from Tokyo Institute of Technology, Japan, in 1989. He started his academic carrier in 1983 at Tokyo Institute of Technology. In 1991, he joined as an associate professor and since 2002 as a professor at the Department of Chemistry and Biomolecular Science, Gifu University, Japan. He has been a professor emeritus, Gifu University, since 2023. His research interests are in nanotechnology, inorganic materials, thin-film fabrication, and material characterization.
(ohya.yutaka.b3@a.gifu-u.ac.jp)

Wulam Tri Wahyuni received her Ph.D. degree from the University of Indonesia, Indonesia, in 2015. From 2012 to 2023, she was an assistant professor at the Chemistry Department, IPB University, Indonesia, and an associate professor since 2023. Her research interests are in analytical chemistry, electroanalysis, and electrochemical sensors.
(wulantriws@apps.ipb.ac.id)